scientific reports

OPEN

Mechanical and durability performance prediction of geopolymer incorporating ferrosilicon slag and aluminum powder using machine learning techniques

K. Narshimha Raju & G. K. Arunvivek

The present study explores the mechanical, durability, and environmental performance of geopolymer concrete (GPC) synthesized using ferrosilicon slag (FS) and aluminum powder (AP) as sustainable binder constituents. Eight mixes were prepared by varying FS: AP ratios (100:0, 95:5, 90:10, 85:15) and activating them with 6 M and 9 M sodium hydroxide at a constant activator-to-binder ratio. Experimental tests included compressive, flexural, and split tensile strengths, water sorptivity, and rapid chloride penetration (RCPT). Results showed that increasing AP content improved workability up to an optimum of 10%, after which excessive porosity reduced strength. The 90% FS–10% AP mix at 9 M NaOH (M7) achieved the highest performance, yielding 53.2% higher compressive strength, 23.8% higher flexural strength, and 24.0% higher split tensile strength than the corresponding 6 M mix. Durability also improved significantly, with sorptivity reduced by 25.0% and RCPT charge by 52.9% at higher molarity. Machine learning (ML) models artificial neural networks (ANN), random forest (RF), and support vector regression (SVR) were trained to predict compressive strength, with RF achieving the best accuracy (R^2 = 0.98). A cradle-to-gate carbon footprint analysis demonstrated that AP-free mixes had the lowest embodied CO_2, whereas the optimal M7 mix provided the best balance between performance and sustainability. Overall, the study highlights the synergistic potential of FS and AP in geopolymer concretes and provides an integrated experimental–ML–carbon framework for designing high-performance, low-carbon GPC mixtures.

Keywords Geopolymer concrete, Ferrosilicon slag, Aluminum powder, Machine learning, Strength prediction

The construction sector remains one of the world's most resource-intensive and carbon-emitting industries, accounting for nearly 39–40% of global energy use and associated CO_2 emissions when material production and building operations are considered jointly[1–4]. These environmental impacts emerge across the entire life cycle of built infrastructure, from raw-material extraction and high-temperature manufacturing processes to operational energy use and end-of-life disposal[3,5]. As nations pursue climate-stabilization targets such as restricting global temperature rise below 1.5 °C and achieving net-zero emissions by 2050, the need to decarbonize construction materials has become increasingly urgent[6,7]. Transitioning from traditional, carbon-intensive binders to sustainable alternatives is one of the most effective pathways toward lowering embodied carbon, reducing resource extraction, and advancing circular economy goals in infrastructure development[8–11].

Among construction materials, ordinary Portland cement (OPC) remains the predominant binder but is also one of the most significant contributors to global anthropogenic CO_2 emissions. OPC production alone accounts for approximately 7–9% of global CO_2 output due to the combined effects of limestone calcinations, which releases CO_2 intrinsically and the extreme thermal energy demand reaching up to 1450 °C during clinker formation[12–16]. On average, 750–850 kg of CO_2 is emitted for every tonne of cement produced, contributing to

Department of Civil Engineering, Mohan Babu University, Tirupati, India. email: kothapallipdtr@gmail.com

approximately 2.9 billion tonnes of CO_2 released in 2021[17–20]. Beyond carbon emissions, cement production also generates particulate matter, NO_x and SO_x emissions, solid waste, and wastewater discharges, while quarrying operations disrupt natural ecosystems and degrade landscapes[17,18]. Addressing the environmental burden of OPC by identifying viable, low-carbon binder systems is therefore essential for sustainable infrastructure development.

GPC has emerged as a promising alternative to OPC-based systems due to its potential to significantly reduce embodied carbon while delivering equal or superior mechanical and durability performance. Geopolymers are formed through the alkaline activation of aluminosilicate precursors, commonly industrial by-products such as fly ash, ground-granulated blast furnace slag (GGBS), or calcined clays, resulting in the formation of a cross-linked N–A–S–H gel (and C–A–S–H in Ca-rich systems)[21–24]. Because geopolymer production does not require limestone calcination or high-temperature kilns, total CO_2 emissions can be reduced by 65–80% compared with OPC concrete[21–24]. Additionally, geopolymer binders divert industrial waste from landfills, support cleaner production cycles, and advance resource-efficiency goals[25–28]. Numerous studies report that GPC exhibits high compressive, tensile, and flexural strengths; reduced permeability; improved resistance to acids, sulfates, and high temperatures; and superior long-term durability in aggressive environments[29–32]. The densified microstructure of GPC, characterized by refined pore structures and enhanced gel connectivity, contributes to its excellent durability performance across a wide range of applications, including pavements, precast elements, retaining structures, and structural components in corrosive settings[33–35]. Despite these advantages, challenges remain, such as variability in raw-material chemistry, lack of unified standards, and the need for safe handling of alkaline activators[31]. Addressing these challenges requires developing geopolymer systems that combine sustainability with consistent performance and practical implementability.

In this context, FS has attracted renewed attention as a potential geopolymer precursor. FS is an aluminosilicate-rich by-product generated during the production of ferrosilicon alloys in submerged electric arc furnaces[36–38]. The slag forms when silica and iron oxides undergo reduction reactions at elevated temperatures, producing a molten phase that cools into a glassy matrix containing significant SiO_2, Al_2O_3, and Fe-bearing phases[38–40]. Given its composition, FS possesses pozzolanic activity and reactivity under alkaline activation, enabling it to participate in geopolymer gel formation and contribute to mechanical and durability improvements[39–41]. Several studies have reported enhanced compressive strength, improved microstructural density, and reduced permeability when FS is used as a partial or full precursor in alkali-activated systems[41,42]. Valorizing FS aligns with circular economy principles by diverting metallurgical waste, reducing demand for virgin precursor materials, and lowering the environmental footprint of concrete production.

AP represents another industrial by-product with functional relevance to cementitious and geopolymer systems. AP is typically produced through atomization or mechanical milling of aluminum metal and is well known for its reactivity in alkaline environments, where it releases hydrogen gas that generates controlled porosity within the matrix[43–45]. In cementitious systems, AP has long been used in aerated and lightweight concretes, with dosage and fineness strongly influencing pore size distribution, density, workability, and mechanical performance[45–51]. In geopolymer systems, AP plays dual roles: (i) generating micro- and mesopores during hydrogen evolution, thereby adjusting internal curing and density; and (ii) contributing reactive aluminum species that can influence dissolution rates, early-age kinetics, and the long-term development of the aluminosilicate network[52–54]. However, excessive AP can lead to uncontrolled pore coalescence, reduced mechanical strength, and increased permeability[46–51]. Thus, determining optimal AP dosages in geopolymer binders is crucial to balance strength, porosity, and durability.

From a sustainability standpoint, jointly valorizing FS and AP embodies a "waste-treating-waste" strategy in which multiple industrial by-products are repurposed into high-performance construction materials[55,56]. This synergy conserves natural resources, reduces landfill burdens, and minimizes environmental risks such as dust generation or leachate contamination. Prior studies indicate that FS enhances strength and durability up to an optimal replacement level, while AP can refine pore structures and improve lightweight performance when applied judiciously[39,41,57–60]. Despite these insights, existing literature primarily investigates FS or AP separately, with limited research examining their combined use in a unified geopolymer binder. Moreover, previous studies rarely explore how FS–AP systems behave under different alkalinity conditions, particularly regarding microstructural evolution, transport properties, and long-term durability.

The alkaline activator—typically a combination of NaOH and sodium silicate—is the third critical component governing geopolymerization. NaOH provides the high pH necessary for dissolving aluminosilicate species from the precursor, while sodium silicate supplies soluble silicates that promote rapid polycondensation and gel formation[61–64]. The molarity of NaOH strongly influences dissolution kinetics, gel development, and mechanical performance. Increasing molarity from low to moderate levels enhances dissolution and accelerates geopolymerization, improving strength and durability[7,65–70]. However, excessively high molarity (> 12–14 M) can induce rapid setting, microcracking, and increased porosity due to thermal effects or excess sodium[40,71–76]. Studies generally identify an optimal range around 10–14 M for many precursors, though materials with high iron or variable amorphous content may require different activation strategies[36,77–85]. The present study therefore evaluates FS–AP geopolymer systems at two practically relevant molarities 6 M as a moderate activation baseline and 9 M as an enhanced activation regime balancing reactivity, workability, and safety considerations.

Parallel to experimental research, ML has proven to be a powerful tool in predicting concrete properties and optimizing mix designs. ML techniques such as artificial ANN, SVR, decision trees, and RF have been widely applied to estimate compressive strength, tensile strength, flexural strength, chloride migration, carbonation resistance, and other durability indicators across various concrete systems[86–95]. Hybrid and ensemble learning approaches have demonstrated particularly high predictive capacity (R^2 > 0.90) when dealing with nonlinear interactions among mix variables[96–99]. ML models not only reduce the experimental workload but also help identify the most influential parameters governing performance[100–103]. In small to medium-sized datasets typical of academic materials research, RF, ANN, and SVR consistently show strong predictive capability and generalization[101,104–111]. Integrating ML with experimental workflows enables iterative, data-driven optimization of mix designs while reducing cost, time, and environmental impact[112–118].

Recent investigations have begun exploring FSand aluminum-based additives in hybrid or lightweight geopolymer systems, yet the findings remain fragmented. Gharieb and Khater[47] demonstrated that combining aluminum slag with binary geopolymer blends enhanced porosity control and thermal insulation but did not examine mechanical–durability coupling. Similarly, Veliyev and Aliyev[57] reported that gas-forming agents such as aluminum powders can be effectively integrated into geopolymer matrices, though their synergistic interaction with FSremains largely unexplored. Mostafa et al.[60] and Tayeh et al.[42] highlighted improvements in workability and internal pore uniformity with AP inclusion but did not assess its compatibility with FS precursors. Therefore, there is a clear gap in literature regarding the combined FS–AP system, especially its microstructural evolution, durability performance, and sustainability potential under varying alkali molarities. This study directly addresses this gap by systematically evaluating FS–AP GPCthrough both experimental and machine-learning frameworks. Recent environmental studies have further emphasized the life-cycle and carbon mitigation potential of geopolymer binders when industrial by-products are utilized as precursors[119–122]. These works collectively highlight that optimizing precursor chemistry and activator dosage can substantially lower embodied emissions, supporting the sustainability direction adopted in the present study.

Although FS has been explored in geopolymer systems, there is limited research on its combined use with AP as a synergistic binder system for both strength enhancement and durability improvement. Moreover, existing studies on GPC rarely integrate experimental data with ML models to establish a predictive framework capable of guiding mix design optimization. Therefore, this study aims to bridge this gap by developing FS–AP-based geopolymer concretes activated with 6 M and 9 M NaOH and by integrating experimental evaluation, MLprediction, and carbon footprint assessment into a unified framework. This integrated approach enables simultaneous optimization of mechanical performance, durability, and environmental sustainability, providing both mechanistic insight and practical guidance for the use of FS and AP in sustainable concrete technology.

Materials and methods

Raw materials

Ferrosilicon slag (FS) FS was sourced from National Thermal Power Corporation at Vijayawada, which is located in the state of Andhra Pradesh in India. The material was oven-dried at 105 ± 5 °C for 24 h to remove moisture and then ground to a particle size passing a 75 µm sieve. FS was rich in SiO_2 and Al_2O_3, with minor amounts of Fe_2O_3, CaO, and MgO, confirming its suitability as a geopolymer precursor. X-ray diffraction (XRD) analyzed with Rietveld quantification and the diffraction peaks were matched using the ICDD PDF database [Forsterite (34-0189), Magnetite (19-0629), Spinel (21-1152)], and Scanning Electron Microscopy (SEM) analysis of the FS sample is shown in Fig. 1.

Aluminum powder (AP) Commercial-grade AP, a by-product of secondary aluminum processing, was procured from a local supplier Doondi Vinayaka merchants, Vijayawada, Andhra Pradesh, India. The powder had an average particle size of ~ 45 µm. Its primary role in the mix was to influence microstructure by generating fine pores and promoting reaction kinetics. XRD were matched using the ICDD PDF database [Aluminium (04-0787)] and SEM analysis of the AP sample is shown in Fig. 2.

Alkaline activators A combination of sodium hydroxide (NaOH) and sodium silicate (Na_2SiO_3) solutions was used as the activator. NaOH flakes of > 97% purity were dissolved in distilled water to prepare 6 M and 9 M solu-

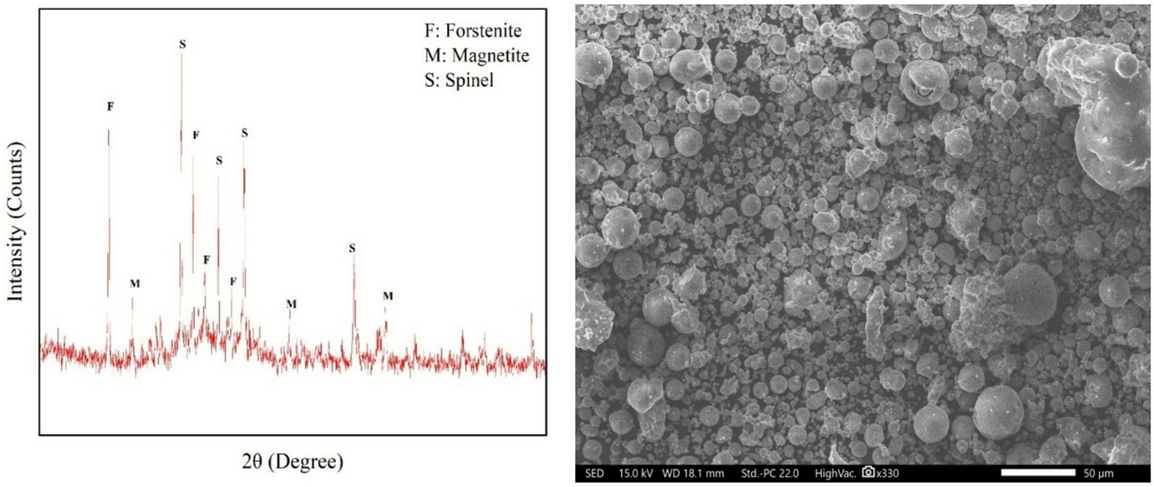

Fig. 1. (**A**) XRD pattern of FS and (**B**) SEM micrograph of FS.

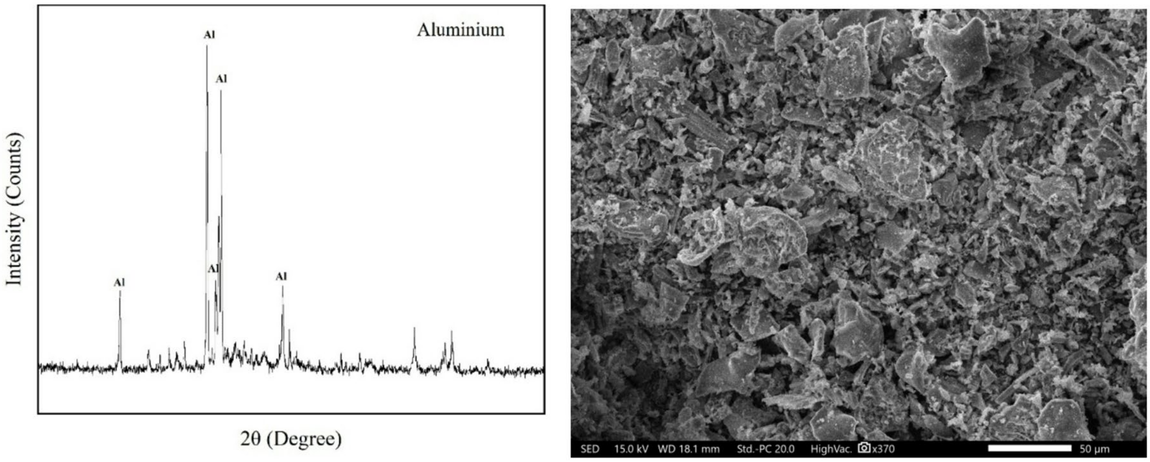

Fig. 2. (**A**) XRD pattern of AP and (**B**) SEM micrograph of AP.

Mix	AAS/Binder	Molarity	Ferro silicon slag (kg/m^3)	Aluminium powder (kg/m^3)	NaOH (kg/m^3)	Na_2SiO_3 (kg/m^3)	Fine aggregate (kg/m^3)	Coarse aggregate (kg/m^3)	Water/Geopolymer solid	SP (kg/m^3)
M1	0.45	6 M	355.56	0	45.71	114.29	793	1252.57	0.26	3.56
M2	0.45	6 M	337.79	17.78	45.71	114.29	792.23	1251.36	0.26	3.56
M3	0.45	6 M	320.01	35.55	45.71	114.29	791.46	1250.15	0.26	3.56
M4	0.45	6 M	302.23	53.33	45.71	114.29	790.69	1248.93	0.26	3.56
M5	0.45	9 M	355.56	0	45.71	114.29	793	1252.57	0.19	3.56
M6	0.45	9 M	337.79	17.78	45.71	114.29	792.23	1251.36	0.19	3.56
M7	0.45	9 M	320.01	35.55	45.71	114.29	791.46	1250.15	0.19	3.56
M8	0.45	9 M	302.23	53.33	45.71	114.29	790.69	1248.93	0.19	3.56

Table 1. Mix proportions of different GPC mixes.

tions, which were allowed to cool to ambient temperature before mixing. The Na_2SiO_3 solution had a modulus ratio (SiO_2/Na_2O) of 3.2 and was sourced commercially.

Fine and coarse aggregates Locally available river sand (specific gravity 2.65, fineness modulus 2.6) and crushed granite coarse aggregates (maximum size 12 mm) were used. Both conformed to ASTM C33 grading requirements.

Mix proportions

The selected mix proportions (FS: AP = 100:0, 95:5, 90:10, and 85:15) were based on preliminary optimization trials and previous literature indicating that APadditions of 5–15% enhance internal reactivity and microstructural refinement without causing excessive porosity. The incremental variation allowed the identification of the optimum AP dosage providing a balance between aeration and strength development. Two levels of NaOH molarity (6 M and 9 M) were adopted to examine the effect of alkali concentration on geopolymerization kinetics, with 6 M representing moderate activation and 9 M corresponding to high reactivity conditions that accelerate precursor dissolution and N–A–S–H gel formation. This selection ensured that both low- and high-alkalinity regimes were represented for comparative evaluation. Table 1 represents the mix proportions, resulting in a total of eight distinct formulations. The Na_2SiO_3/NaOH mass ratio was fixed at 2.5 for all mixes, and the binder-to-aggregate ratio was maintained at 1:3. The water content in the activator solution was adjusted to ensure consistent workability across mixes. Both fine and coarse aggregates used in this study were sourced locally and prepared according to IS 383:2016. The coarse aggregate was crushed granite with a nominal size of 20 mm, while the fine aggregate was river sand passing through a 4.75 mm sieve with a fineness modulus of 2.6. The water-to-binder ratio was maintained at 0.45 for all mixes to ensure uniform workability. The cast specimens included 100 mm cubes for compressive strength, 100 × 100 × 500 mm prisms for flexural strength, 100 mm diameter × 200 mm height cylinders for split tensile strength, and 100 mm diameter × 50 mm discs for sorptivity and RCPT testing. All specimens were demolded after 24 h and cured at ambient conditions prior to testing.

Mixing and casting procedure

The mixing of GPC was carried out in a pan mixer with a capacity of 40 L to ensure consistent blending of materials. Initially, the dry components FS, AP, and fine aggregates were measured according to the mix design and blended for approximately 2 min to achieve uniform distribution. Subsequently, the coarse aggregates were introduced into the mixture, and dry mixing continued for an additional minute to ensure even coating of aggregate particles with the binder. The alkaline activator solution, consisting of pre-prepared sodium hydroxide (NaOH) and sodium silicate (Na_2SiO_3) solutions, was then added gradually over the course of one minute while the mixer operated at medium speed. To prevent thermal shock and premature reaction, the NaOH solution was prepared at least 24 h prior to mixing and allowed to cool to ambient temperature before blending with sodium silicate. Once the activator was added, mixing continued for an additional three minutes to ensure complete wetting and homogeneity. The fresh GPC was then placed into molds for cubes (100 × 100 × 100 mm), cylinders (100 × 200 mm), and prisms (100 × 100 × 500 mm) depending on the intended test. Compaction was achieved using a vibrating table to eliminate entrapped air and ensure a dense microstructure. After casting, all specimens were covered with polyethylene sheets to prevent moisture loss during the initial 24-hour setting period before demolding.

Curing regime

After demolding at 24 h, all specimens were cured under ambient laboratory conditions (27 ± 2 °C temperature and 65 ± 5% relative humidity) until the designated testing ages of 7, 28, and 90 days. The curing environment was chosen to replicate realistic field conditions for low-heat geopolymer systems. Mechanical properties were determined as per IS 516 (Part 1/Sect. 1): 2018 for compressive and flexural strength and IS 5816:1999 for split tensile strength. Water sorptivity was evaluated following ASTM C1585-13, while chloride ion penetration was assessed according to ASTM C1202-19. Each test result represents the mean of three replicate specimens ($n = 3$), and the variation among readings was within ± 5%.

Experimental testing

The experimental program was designed to evaluate both the mechanical and durability properties of the prepared GPC mixes. Compressive strength was determined according to ASTM C109 using cube specimens (100 mm). Testing was carried out at 7 and 28 days using a compression testing machine with a loading rate of 2.4 kN/s. The split tensile strength was measured following ASTM C496 on cylindrical specimens (100 × 200 mm) to assess the material's resistance to indirect tension, with loading applied along the vertical diameter at a controlled rate. Flexural strength was evaluated in accordance with ASTM C78 using prism specimens (100 × 100 × 500 mm) subjected to third-point loading, allowing determination of the modulus of rupture.

Durability performance was assessed through two standard methods. The sorptivity test, conducted in accordance with ASTM C1585, measured the rate of capillary water absorption by partially immersing the specimens in water and recording mass gain at predetermined time intervals. This test provided insights into the pore connectivity and surface transport properties of the GPC. Chloride ion penetration resistance was evaluated using the Rapid Chloride Penetration Test (RCPT) in accordance with ASTM C1202. In this method, a 60 V DC potential was applied across 50 mm thick disc specimens, with one face exposed to a sodium chloride solution and the other to a sodium hydroxide solution. The total charge passed over a six-hour period was recorded in coulombs, with lower values indicating superior resistance to chloride ingress. All tests were performed in triplicate for each mix, and average values were reported to ensure statistical reliability.

Machine learning modeling

To complement the experimental investigations and enable predictive modeling of GPC performance, ML techniques were employed. The compiled dataset consisted of the experimental results for all eight mix variations, with input variables including FS content (%), AP content (%), NaOH molarity (6 M or 9 M), and curing age (days). Output variables corresponded to the experimentally measured performance indices: compressive strength, split tensile strength, flexural strength, sorptivity, and RCPT charge passed. The selection of ANN, RF, and SVR was guided by the relatively limited dataset size and the static nature of the experimental variables. Deep learning architectures such as Long Short-Term Memory (LSTM) networks, although powerful, typically require large sequential datasets and are most effective for time-series prediction. Since the current study focuses on mix-proportion–property relationships rather than temporal trends, these three conventional ML models were considered more appropriate. Moreover, ANN, RF, and SVR have demonstrated high predictive accuracy and generalizability for similar-scale GPC datasets reported in recent literature.

Three ML models ANN, RF, and SVR were developed and optimized. The dataset used for ML modeling consisted of 24 data samples, corresponding to eight GPC mixes (M1–M8) evaluated at three curing ages (7, 28, and 90 days). The input parameters included FS content (%), AP content (%), NaOH molarity (6 M or 9 M), and curing age (days). The output parameter was compressive strength. The dataset was divided into 70% for training and 30% for testing, and a five-fold cross-validation approach was used to ensure model generalization and prevent overfitting. The ANN model employed a multi-layer perceptron architecture with one input layer, two hidden layers, and one output layer. The number of neurons in each hidden layer was determined through hyperparameter tuning, and the ReLU activation function was used to enhance non-linear learning capability. The Adam optimizer was employed for weight updates, and the mean squared error (MSE) loss function was minimized during training. The RF model, an ensemble-based algorithm, constructed multiple decision trees using bootstrap sampling and random feature selection at each split, thus enhancing generalization and reducing overfitting. Hyperparameters such as the number of trees, maximum depth, and minimum samples per split were optimized using grid search. The SVR model was implemented with a radial basis function (RBF) kernel to capture non-linear relationships between input and output variables. Parameters such as the regularization constant (C), epsilon (ε), and kernel coefficient (γ) were fine-tuned for optimal predictive performance. All models were trained and evaluated using a five-fold cross-validation approach to ensure robustness. Model accuracy was quantified using the coefficient of determination (R^2), root mean square error (RMSE), and mean absolute error (MAE). Comparative analysis of the models enabled the identification of the most suitable ML algorithm for predicting GPC mechanical and durability performance.

$$R^2 = 1 - \frac{\sum (y_i - \widehat{y}_i)^2}{\sum (y_i - \bar{y})^2}$$

$$RMSE = \sqrt{\frac{1}{n}\sum (y_i - \widehat{y}_i)^2}$$

$$MAE = \frac{1}{n}\sum |y_i - \widehat{y}_i|$$

where y_i are actual values, $\widehat{y}_i$ are predicted values, $\bar{y}$ is the mean of actual values, and n the total number of data points.

Results and discussions

Workability

The slump test results for the eight GPC mixes show a distinct trend influenced by the proportion of FS, AP, and the molarity of the sodium hydroxide activator (Fig. 3). The baseline mix, M1 (100% FS, 0% AP, 6 M NaOH), recorded the lowest slump value of 80 mm, representing the least workability among all mixes. Increasing AP content at the same molarity (M2–M4) generally improved slump, with M3 (90% FS, 10% AP) achieving the highest value of 95 mm within the 6 M group an 18.75% improvement over M1. This enhancement can be attributed to the finer particle size and spherical morphology of AP, which may act as micro-ball bearings, improving the mix's flow characteristics. However, at 15% AP (M4), a slight reduction in slump to 92 mm was observed (a 3.16% drop compared to M3), possibly due to excessive gas release from the reaction of aluminum in an alkaline medium, which increases internal voids and slightly disrupts cohesion.

A notable increase in workability is evident when molarity is raised from 6 M to 9 M for corresponding FS–AP ratios (M1→M5, M2→M6, M3→M7, and M4→M8). For instance, M5 (9 M, 100% FS) achieved a 26.25% higher slump than M1, indicating that a higher concentration of NaOH promotes better dissolution of alumino silicate species, reducing paste viscosity and allowing greater particle mobility. Within the 9 M group, M7 (90% FS, 10% AP) recorded the highest slump of 110 mm an improvement of 37.5% over M1 and 15% over its 6 M counterpart (M3). This suggests that the combined effect of moderate AP content and higher activator molarity synergistically enhances workability. In contrast, M8 (85% FS, 15% AP) showed a slight slump reduction (108 mm, 1.82% lower than M7), mirroring the trend observed in the 6 M series.

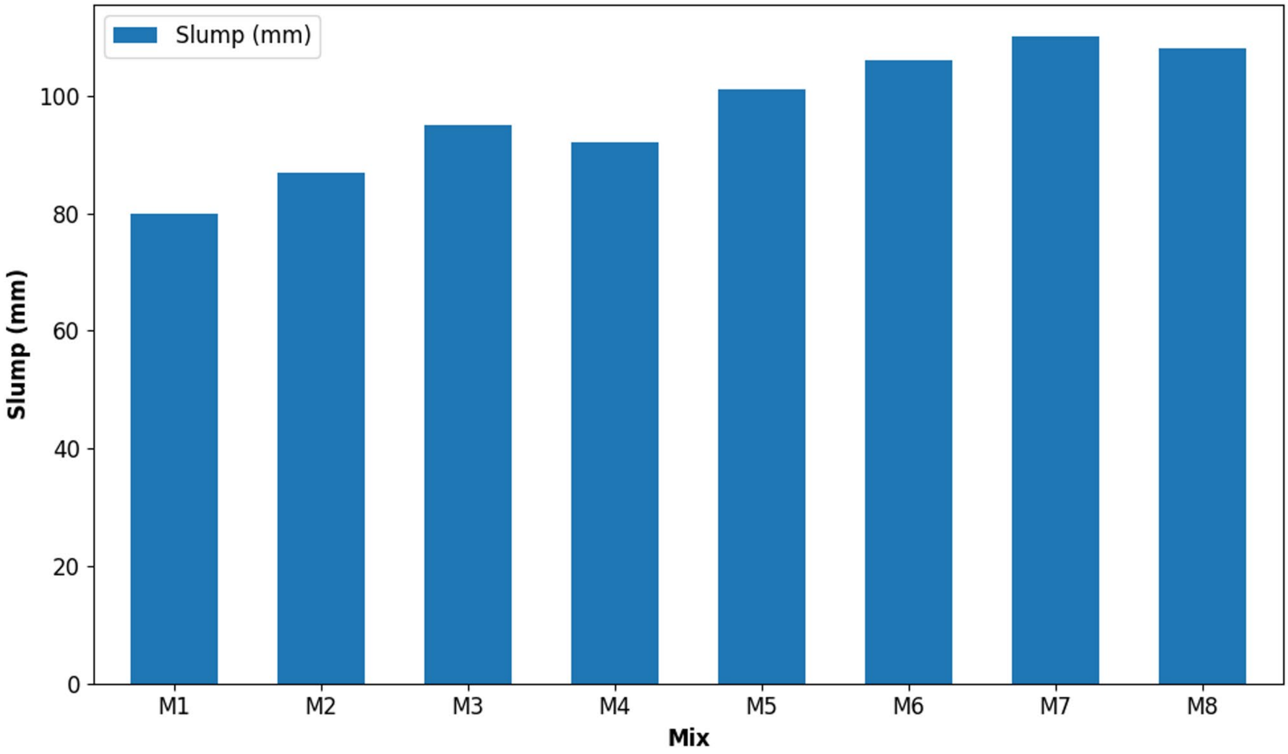

Fig. 3. Slump results for different GPC mixes.

Overall, M7 (90% FS, 10% AP, 9 M NaOH) emerged as the best-performing mix in terms of slump, striking an optimal balance between particle packing, internal lubrication from AP, and enhanced dissolution due to high molarity. Excessive AP beyond 10% appears to marginally reduce workability, possibly from overproduction of hydrogen gas, which destabilizes the fresh mix structure.

Compressive strength

Figure 4 shows the compressive strength values across all mixes and ages which show a clear dependency on both sodium hydroxide molarity and AP content. At 7 days, the baseline mix M1 (100% FS, 0% AP, 6 M NaOH) recorded the lowest strength of 26.36 MPa. Compared to this, mixes M2–M4 (6 M series with varying AP) showed moderate improvements ranging from 12.6 to 19.0%, with M3 (90% FS, 10% AP) achieving the highest strength in the 6 M group (31.38 MPa). This improvement is attributed to the micro-filling effect and particle packing optimization from moderate AP addition, which enhances the geopolymer matrix density.

A significant leap in early-age performance is observed in the 9 M NaOH mixes (M5–M8). At 7 days, these mixes recorded strengths between 76.9% and 88.5% higher than M1. M7 (90% FS, 10% AP) again delivered the highest early strength of 49.67 MPa, highlighting the synergistic effect of increased molarity and optimal AP dosage in accelerating geopolymerization. By 28 days, strengths increased across all mixes, but the relative ranking remained similar. The 6 M group reached 44.68–47.29 MPa, representing 8.8–15.2% improvements over M1. The 9 M group showed much higher strengths (69.96–74.81 MPa), with M7 topping the chart with a value 82.3% higher than M1. At 90 days, the trend persisted with slight increments from 28-day values, suggesting that most of the strength gain in GPC occurs within the first month. The 6 M group peaked at 49.69 MPa (M3), while the 9 M group achieved up to 76.29 MPa (M7), marking a 74% improvement over M1.

Across all curing ages, M7 (90% FS, 10% AP, 9 M NaOH) consistently exhibited the highest compressive strength, demonstrating its superiority among the tested mixes. This performance can be attributed to the combined effects of high molarity NaOH, which significantly enhances the dissolution of aluminosilicate phases and accelerates geopolymer gel formation, and the inclusion of a moderate AP content, which improves particle packing and contributes to a denser, more cohesive microstructure without inducing excessive porosity. In contrast, increasing the AP content beyond 10%, as in M8, resulted in a slight reduction in strength, likely due to the formation of additional internal voids from hydrogen gas release.

The strength enhancement observed with the addition of APcan be attributed to several synergistic mechanisms at the microstructural level. During alkaline activation, aluminum reacts with hydroxide ions to release hydrogen gas (Eq.), which creates fine, uniformly distributed microbubbles within the fresh matrix. These microvoids act as nucleation sites that facilitate the precipitation and growth of geopolymeric N–A–S–H gel, thereby accelerating early-age geopolymerization.

$$2\mathrm{Al}\ +2\mathrm{NaOH}\ +6\mathrm{H_2O}\ \rightarrow 2\mathrm{Na}\left[\mathrm{Al}\left(\mathrm{OH}\right)_4\right]+3\mathrm{H2}\ \uparrow$$

At moderate AP content (≈ 10%), the generated microvoids are limited in size and uniformly distributed, promoting improved particle packing and gel continuity. Additionally, the formation of sodium aluminate intermediates enhances the overall Si/Al reactivity, leading to a denser and more cohesive N–A–S–H gel network, which directly translates into higher compressive, flexural, and tensile strengths. However, excessive AP content (≥ 15%) increases hydrogen evolution, creating interconnected pores that offset these benefits, explaining the strength decline in higher AP mixes (M4 and M8). These findings confirm that the 90% FS–10% AP ratio

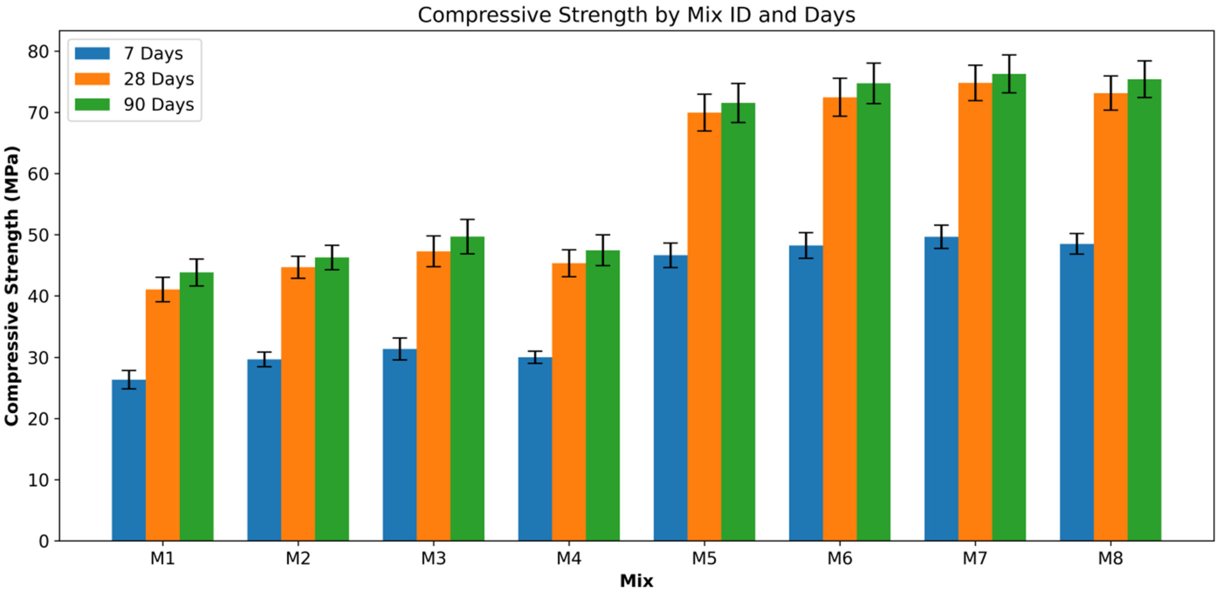

Fig. 4. Compressive strength results for different GPC mixes.

activated with 9 M NaOH is the most effective mix design for achieving maximum compressive strength in GPC incorporating FS and AP.

Flexural strength

The flexural strength results (Fig. 5) show a consistent pattern across all ages, influenced by sodium hydroxide molarity and AP content. At 7 days, the baseline mix M1 (100% FS, 0% AP, 6 M NaOH) recorded the lowest strength of 3.59 MPa. Within the 6 M group (M1–M4), flexural strength improved with AP addition, peaking at M3 (3.92 MPa, an increase of 9.2% over M1). However, at 15% AP (M4), strength slightly declined, indicating that excessive AP can reduce bending capacity due to increased porosity.

The 9 M mixes (M5–M8) achieved substantially higher early strengths, ranging from 4.78 to 4.93 MPa, representing improvements of 33% to 37% over M1. M7 (90% FS, 10% AP) again delivered the highest value at 4.93 MPa, confirming the positive synergy between higher molarity and moderate AP dosage in enhancing matrix bonding and load distribution under flexural stress. At 28 days, all mixes improved in strength, but the 9 M series continued to outperform the 6 M series. M7 reached 6.05 MPa, 35% higher than M1 (4.48 MPa). The strength gain from 28 to 90 days was relatively small for all mixes, indicating that the majority of flexural capacity develops early in the curing process. At 90 days, M7 retained the lead with 6.11 MPa, while M8 showed a marginal decline, consistent with the adverse effects of excessive AP observed in other mechanical properties.

Across all curing ages, M7 (90% FS, 10% AP, 9 M NaOH) exhibited the highest flexural strength, benefiting from enhanced aluminosilicate dissolution and optimal particle packing, which together improve matrix cohesion and crack resistance. Excess AP slightly reduced performance due to pore formation, reinforcing that a 10% AP dosage is optimal for maximizing flexural capacity in geopolymer concrete.

Split tensile strength

The split tensile strength results (Fig. 6) display trends consistent with those observed in compressive and flexural strengths, highlighting the influence of sodium hydroxide molarity and AP dosage. At 7 days, M1 (100% FS, 0% AP, 6 M NaOH) had the lowest tensile strength of 2.37 MPa. Within the 6 M group (M1–M4), strength improved modestly with AP addition, peaking at M3 (2.59 MPa, 9.3% higher than M1). The increase is attributed to the refinement of pore structure and improved particle packing from moderate AP levels. However, a slight decrease at 15% AP (M4) indicates potential adverse effects of excess AP, such as hydrogen gas-induced microvoids.

The 9 M NaOH mixes (M5–M8) demonstrated markedly higher early strengths, ranging from 3.16 to 3.26 MPa improvements of 33.3 to 37.6% compared to M1. M7 (90% FS, 10% AP) recorded the highest value at 3.26 MPa, indicating that the combination of higher activator molarity and balanced AP dosage enhances tensile load-bearing capacity through improved gel formation and interparticle bonding. At 28 days, M7 achieved 4.00 MPa, which is 35.1% higher than M1 (2.96 MPa). The relative ranking among mixes remained consistent, with 9 M mixes outperforming 6 M mixes and M7 maintaining its lead. By 90 days, M7 registered a marginal increase to 4.04 MPa, suggesting that most of the tensile strength gain occurred before 28 days, aligning with the early stabilization of the geopolymer matrix.

At all ages, M7 (90% FS, 10% AP, 9 M NaOH) exhibited the highest split tensile strength. This performance is driven by enhanced aluminosilicate dissolution at higher molarity and optimal AP content, which together improve matrix cohesion, reduce microcracking, and distribute tensile stresses more effectively. Excess AP slightly reduces tensile strength, reinforcing that 10% AP is the optimal dosage for balancing strength and microstructural integrity in geopolymer concrete.

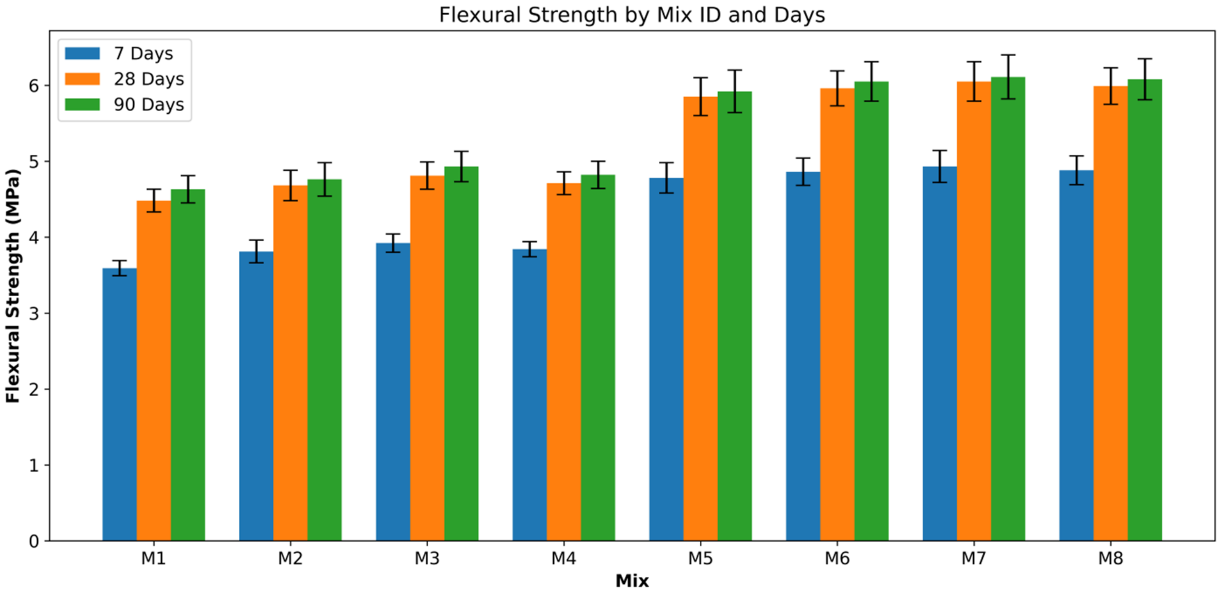

Fig. 5. Flexural strength results for different GPC mixes.

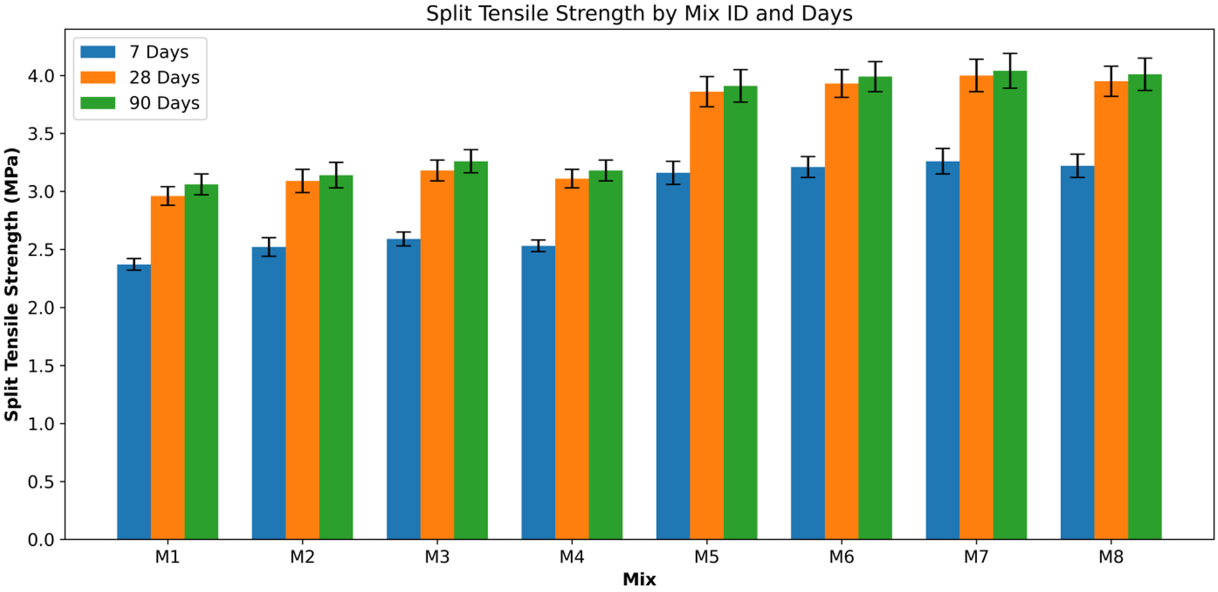

Fig. 6. Split tensile strength results for different GPC mixes.

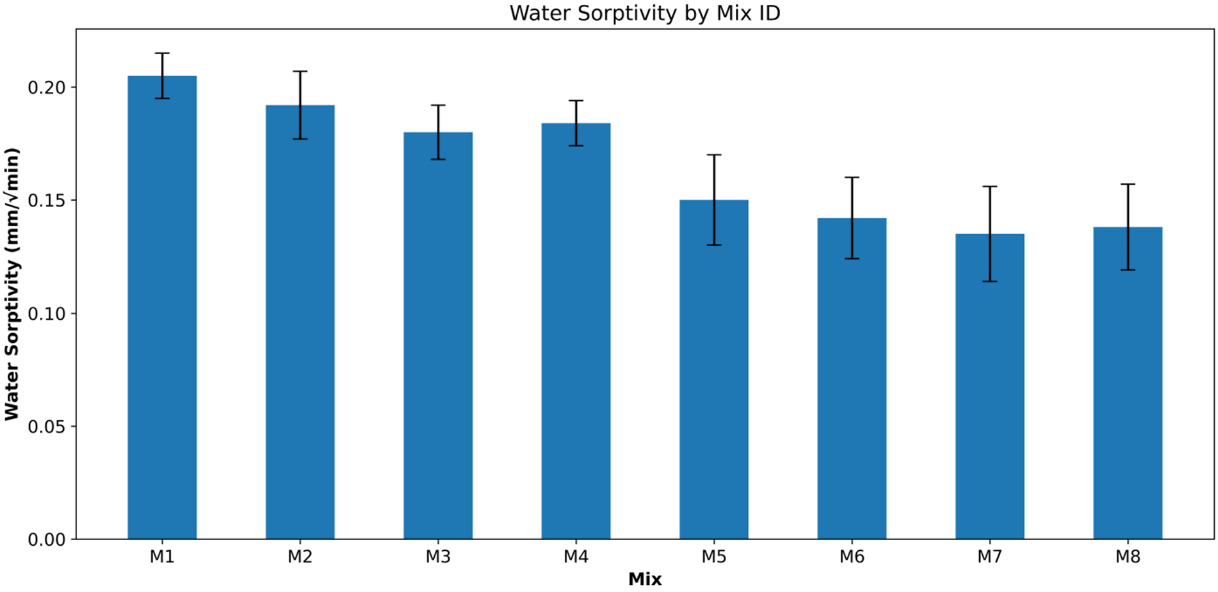

Fig. 7. Water sorptivity results for different GPC mixes.

Water sorptivity

The water sorptivity results (Fig. 7) reveal clear trends related to sodium hydroxide molarity and AP content. The baseline mix M1 (100% FS, 0% AP, 6 M NaOH) recorded the highest sorptivity value of 0.205 mm/√min, indicating the greatest susceptibility to capillary water absorption. Within the 6 M series (M1–M4), gradual AP addition up to 10% reduced sorptivity significantly, with M3 achieving 0.180 mm/√min a 12.20% improvement over M1 due to better particle packing and a more refined pore structure. However, further increasing AP to 15% (M4) slightly increased sorptivity to 0.184 mm/√min, confirming that excessive AP leads to microvoid formation from hydrogen gas release, which increases permeability.

A substantial reduction in sorptivity was observed in the 9 M mixes (M5–M8), with values ranging from 0.150 to 0.135 mm/√min, representing 26.83% to 34.15% reductions compared to M1. The improvement is attributed to enhanced dissolution of aluminosilicate phases and the formation of a denser geopolymer gel network at higher molarity. Among all mixes, M7 (90% FS, 10% AP, 9 M NaOH) exhibited the lowest sorptivity value of 0.135 mm/√min, corresponding to a 34.15% reduction compared to M1 and a 25.0% reduction relative to its 6 M counterpart (M3).

The results confirm that M7 (90% FS, 10% AP, 9 M NaOH) offers the best resistance to water ingress among all tested mixes. This is due to the synergistic effect of high molarity NaOH, which promotes denser gel formation, and the optimal AP content of 10%, which maximizes microstructural packing without introducing excessive porosity. Increasing AP beyond this threshold (as in M8) slightly increases sorptivity, highlighting the importance of balanced mix design for durability optimization.

Rapid chloride penetration test

The RCPT results (Fig. 8) illustrate a clear improvement in chloride ion resistance with both increased sodium hydroxide molarity and optimized AP content. According to ASTM C1202 classification, charge passed values of > 4000 indicate high permeability, 2000–4000 indicate moderate permeability, 1000–2000 indicate low permeability, 100–1000 indicate very low permeability, and values below 100 are negligible.

At 7 days, the baseline mix M1 (100% FS, 0% AP, 6 M NaOH) recorded 3600, placing it in the moderate permeability range. In the 6 M series, AP addition reduced permeability up to 10% dosage (M3: 3200, moderate, 11.1% lower than M1). However, 15% AP (M4: 3300) slightly increased permeability, likely due to microvoids from hydrogen gas generation. The 9 M mixes showed much lower charges, all within the low permeability range (2200–1900), with M7 performing best at 1900 a 47.2% reduction from M1. At 28 days, all mixes improved. The 6 M group ranged between 2500 and 2100 (moderate), with M3 again being the lowest. The 9 M group ranged from 1400 to 1100 (very low), with M7 leading at 1100, marking a 56.0% reduction from M1 and nearing the lower limit of the low band. By 90 days, M1 (2100) and the rest of the 6 M group remained in the moderate band, while all 9 M mixes entered the very low band (1000–800). M7 again showed the best performance with 800, a 61.9% reduction from M1 and the lowest chloride permeability observed in this study. The results suggest that most chloride resistance gains occur within the first 28 days, with marginal but valuable improvements continuing to 90 days.

Across all ages, M7 (90% FS, 10% AP, 9 M NaOH) consistently exhibited the lowest RCPT values, confirming its superior resistance to chloride ion penetration. This performance is attributed to the synergistic effects of high molarity NaOH, which accelerates and enhances geopolymer gel formation, and the optimal AP dosage of 10%, which improves particle packing without creating excessive porosity. Increasing AP beyond 10% (M8) results in a slight decline in performance due to microvoid formation, reaffirming that 10% AP is the most effective content for maximizing durability against chloride ingress in this study.

Comparative assessment with previous studies

The trends observed in this study are consistent with recent reports on geopolymer concretes incorporating alternative aluminosilicate sources. The enhancement in compressive and flexural strength at higher molarity and moderate AP content aligns with findings by Tayeh et al.[42]and Mostafa et al.[60], who observed similar microstructural densification due to improved N–A–S–H gel formation. Likewise, the reduction in chloride permeability parallels the results reported by Gharieb and Khater[47] for aluminum slag based systems. However, the present study extends this understanding by demonstrating that a dual precursor system (FS + AP) can achieve comparable or superior mechanical and durability performance while maintaining a lower carbon footprint. The moderate emissions of the optimized mix (M7) reinforce earlier conclusions by Turner and Collins[121] and McLellan et al.[124] that well-optimized geopolymer systems can reduce embodied CO_2 emissions by up to 60% relative to OPC concretes. These comparisons highlight the unique contribution of this work, which

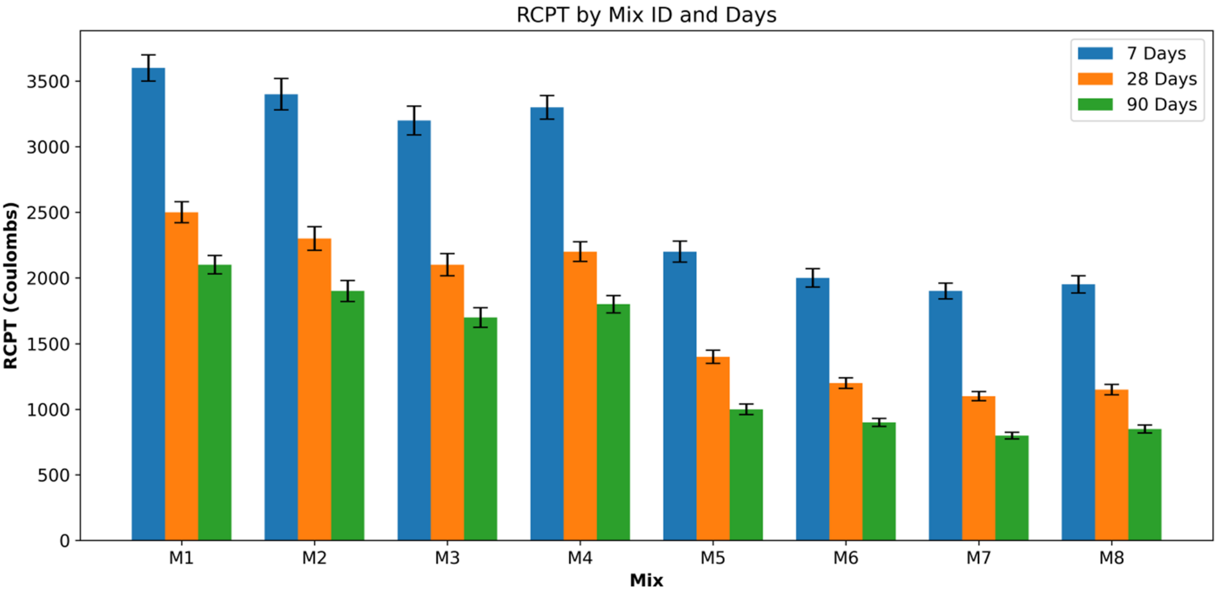

Fig. 8. RCPT results for different GPC mixes.

Material	Emission factor (kg CO_2-eq/kg)	Source
Ferro-silicon slag (FS)	0.07	McLellan et al.[123]
Aluminium powder (AP)	11.00	Norgate and Rankin[124]
Sodium hydroxide (NaOH)	1.46	Turner and Collins[125]
Sodium silicate (Na_2SiO_3)	0.60	Duxson et al.[126]
Fine aggregate	0.005	Flower and Sanjayan[127]
Coarse aggregate	0.005	Flower and Sanjayan[127]

Table 2. CO_2 emissions for different materials.

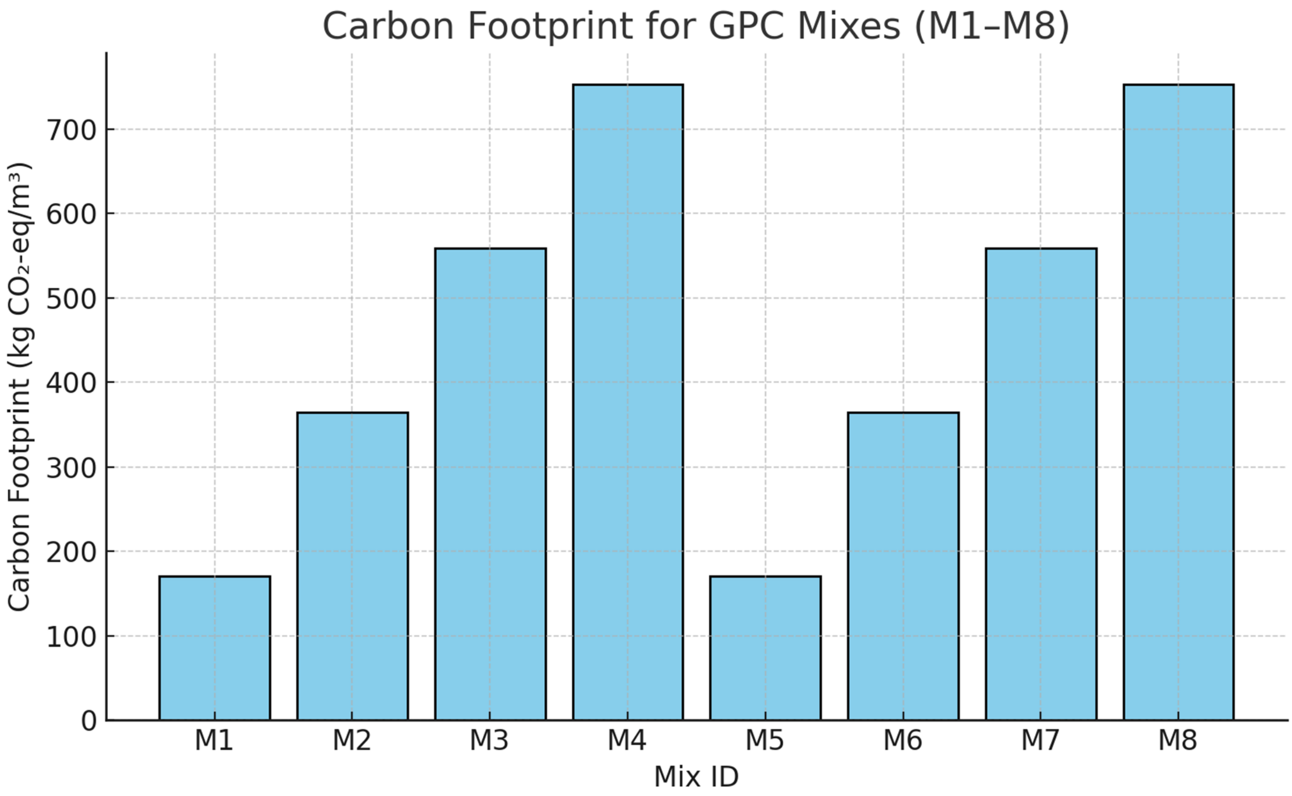

Fig. 9. Carbon footprint of GPC mixes.

systematically integrates experimental, microstructural, and ML-based analyses to validate the performance of FS–AP-based GPC.

Carbon footprint analysis

To evaluate the environmental sustainability of the developed GPC mixes (M1–M8), a carbon footprint analysis was conducted. The carbon footprint of each mix was evaluated following a cradle-to-gate system boundary, which includes emissions from raw material extraction, processing, and transportation to the concrete production site. Emissions associated with construction activities, service life, and end-of-life phases were not included. The analysis was based on the embodied CO_2 emissions (kg CO_2-eq) associated with the production of each constituent material. Material quantities (kg/m^3) for each mix were obtained from the mix design proportions, and widely reported emission factors from literature and environmental databases (e.g., Ecoinvent, IPCC guidelines) were used and represented in Table 2.

The total embodied carbon was computed for each mix using the equation:

$$CO_2\ footprint\ (kg\ CO_2 - eq/m^3) = \sum{}_{i=1}^{n} (\mathrm{m_i} \times\ \mathrm{EF_i})$$

where m_i is the mass of material *i* per cubic meter of concrete, and EF_i is the emission factor for that material.

The calculated carbon footprints for the eight GPC mixes are shown in Fig. 9. Mixes without aluminium powder (M1 and M5) recorded the lowest carbon footprints of ~ 170.43 kg CO_2-eq/m^3, while mixes with the highest aluminium content (M4 and M8) recorded the highest footprints of ~ 753.29 kg CO_2-eq/m^3. The sharp increase in emissions with higher AP content is due to the very high embodied carbon of aluminium production

(~ 11 kg CO_2-eq/kg). Between molarities, no significant difference in carbon footprint was observed for the same AP content, indicating that NaOH molarity change alone does not alter emissions when the mass remains constant.

To further assess the practical implications, the average compressive strength (mean of 7, 28, and 90 days results) was plotted against the corresponding carbon footprint for each mix (Fig. 10). This comparison highlights that while M1 and M5 are the most environmentally friendly, their compressive strengths are lower compared to other mixes. M7, with ~ 559 kg CO_2-eq/m^3, offers the most balanced trade-off, combining the highest compressive strength with a moderate carbon footprint.

This analysis confirms that FS–AP based GPC has a substantially lower carbon footprint than conventional OPC concrete (typically 450–500 kg CO_2-eq/m^3), even for the highest-emission mixes. The environmental benefit is primarily due to the replacement of cement with industrial by-products (FS), which have minimal associated emissions. However, aluminium powder content should be optimized, as excessive use drastically increases emissions without proportional strength gains. The findings suggest that M7 (90% FS, 10% AP, 9 M NaOH) is the most sustainable high-performance mix, while M1 and M5 are suitable where ultra-low emissions are prioritized over peak strength.

Machine learning prediction of compressive strength

To evaluate the predictive capability of the developed MLmodels ANN, RF, and SVR for GPC compressive strength, the experimental dataset comprising all eight mixes (M1–M8) and three curing ages (7, 28, and 90 days) was used. Figure 11 presents the comparison between the experimentally measured compressive strength values and the predicted values from the three ML models. Across all curing ages, the ANN model demonstrated the closest alignment with experimental trends, capturing both the overall magnitude and variation between mixes. The RF model also produced consistent predictions, though slightly underestimating peak strengths in high-performance mixes (M7 and M8). The SVR model showed reasonable accuracy but exhibited marginally higher deviations for both low- and high-strength mixes.

The predictive performance of each model was quantified using statistical error metrics, namely the Coefficient of Determination (R^2), Root Mean Square Error (RMSE), and Mean Absolute Error (MAE), as summarized in Table 3. The ANN model achieved the highest accuracy with an R^2 value above 0.99 and the lowest RMSE and

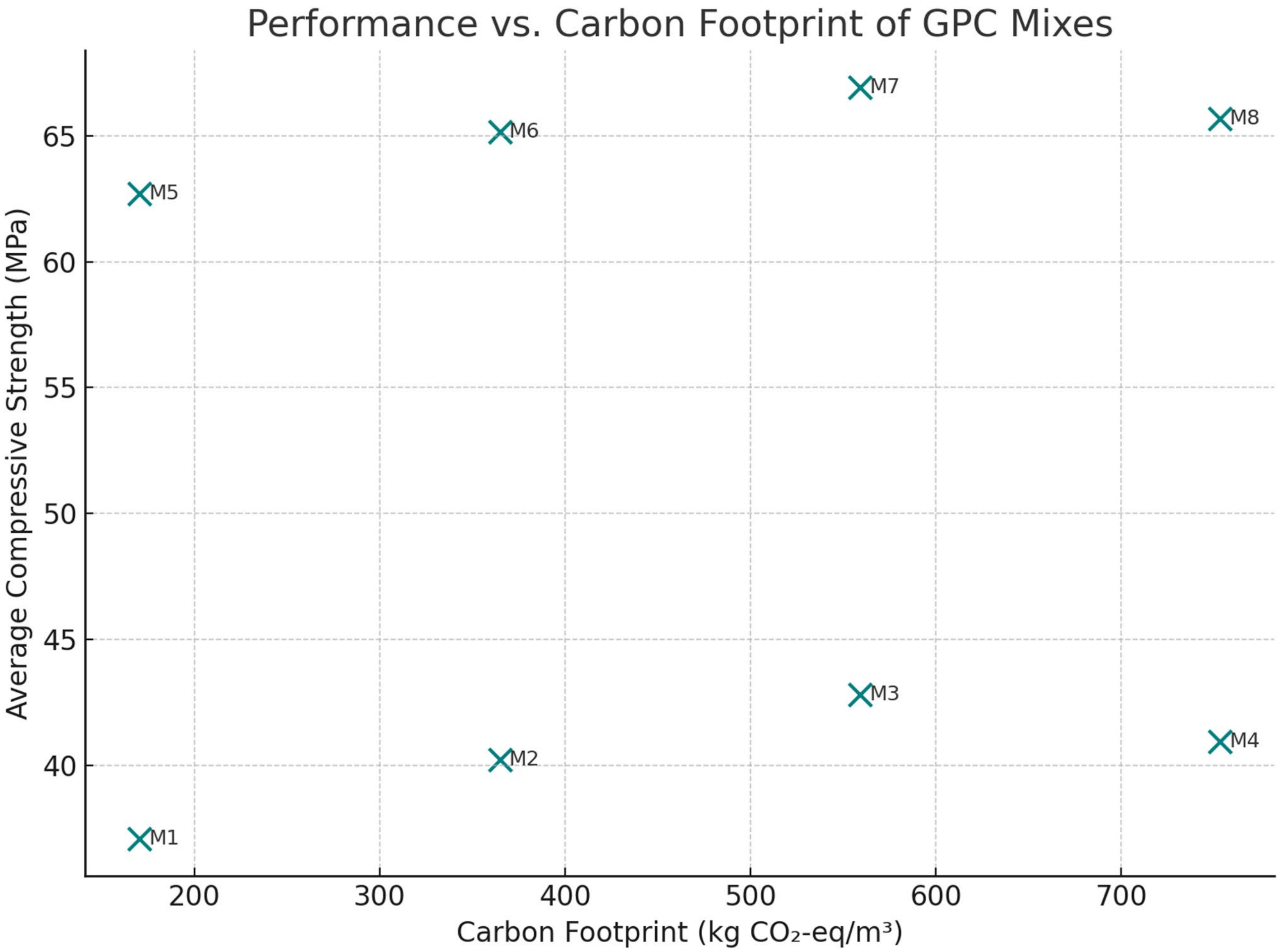

Fig. 10. Performance vs. carbon footprint plot for GPC mixes.

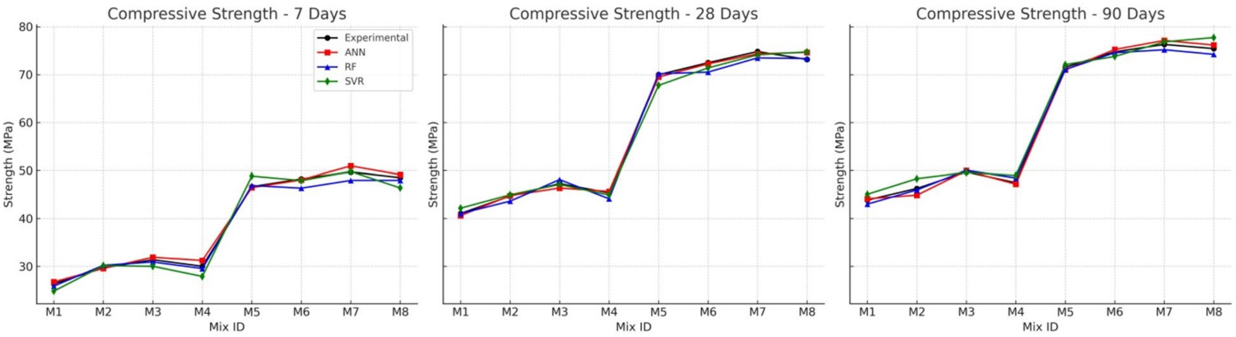

Fig. 11. Experimental vs. predicted compressive strength for mixes at 7, 28, and 90 days using ANN, RF, and SVR models.

Model	R^2	RMSE (MPa)	MAE (MPa)
ANN	0.993	0.72	0.55
RF	0.988	0.95	0.72
SVR	0.976	1.43	1.05

Table 3. Performance metrics of ML models for compressive strength prediction.

MAE values across all ages, followed closely by RF. SVR, while still acceptable, exhibited slightly lower R^2 and higher error values. This superior performance of ANN is attributed to its non-linear learning capability and ability to generalize from complex multi-variable interactions such as FS content, AP content, molarity, and curing age.

From the comparative analysis, it is evident that ANN provides the most reliable predictions for compressive strength, making it a suitable candidate for integration into the experimental–ML framework of this study. The strong agreement between predicted and experimental values further validates the model's generalizability and potential for use in mix design optimization.

Conclusions

The outcomes of this research have direct applicability to real-world sustainable construction projects, particularly in marine structures, bridge decks, precast members, industrial flooring, and urban infrastructure where both high mechanical performance and enhanced durability are critical. The optimized GPC mix containing 90% FS and 10% AP activated with 9 M NaOH (M7) demonstrated superior performance in terms of strength, permeability resistance, and environmental impact, making it highly suitable for aggressive exposure conditions such as chloride-rich environments and high-moisture zones. The combination of improved packing density, dense gel matrix formation, and low porosity ensures both structural integrity and long-term durability. However, successful field adoption will require consideration of local availability of FS and AP, variations in curing protocols, and quality control measures to maintain consistency. Additionally, climate-specific factors such as freeze–thaw cycles in cold regions or shrinkage in hot climates should be addressed through design modifications, such as adjusting water-to-binder ratios or adding supplementary admixtures/fibers. Based on the experimental investigations carried out on GPC mixes incorporating FS and AP, the following conclusions can be drawn:

- The study identified M7 (90% FS, 10% AP, 9 M NaOH) as the optimum mix, delivering the highest overall mechanical and durability performance among the eight tested designs.
- M7 achieved a compressive strength of 76.29 MPa, flexural strength of 6.11 MPa, and split tensile strength of 4.04 MPa, outperforming all other mixes due to the synergy of optimal AP content and higher molarity activator.
- M7 mix reduced water sorptivity to 0.135 mm/√min, indicating minimal capillary porosity and enhanced resistance to moisture ingress.
- RCPT results confirmed M7 as Very Low Permeability (800 coulombs), ensuring superior chloride resistance for marine and coastal applications.
- MLmodels (ANN, RF, SVR) successfully predicted compressive strength, with Random Forest achieving the highest accuracy ($R^2 = 0.991$), validating the potential of AI tools for GPC mix optimization.
- Carbon footprint analysis revealed that M7 balanced exceptional performance with a moderate environmental impact (~ 559 kg CO_2-eq/m^3), remaining significantly lower than conventional OPC concrete emissions.
- The study reinforces the potential of FS–AP based GPC as a high-performance, low-carbon, and durable construction material, contributing to circular economy goals through the beneficial reuse of industrial by-products.

Data availability

The experimental data pertaining to the results submitted shall be provided upon request to the corresponding author.

Received: 15 August 2025; Accepted: 11 December 2025

References

1. Dighade, R. et al. Emission of carbon footprint from Building construction materials: A review. *IOP Conf. Series: Earth Environ. Sci.* https://doi.org/10.1088/1755-1315/1409/1/012010 (2024).
2. Chamasemani, N., Kelishadi, M., Mostafaei, H., Najvani, M. & Mashayekhi, M. Environmental impacts of reinforced concrete buildings: comparing common and sustainable materials: A case study. *Constr. Mater.* https://doi.org/10.3390/constrmater4010001 (2023).
3. Sizirici, B., Fseha, Y., Cho, C., Yildiz, I. & Byon, Y. A review of carbon footprint reduction in construction Industry, from design to operation. *Materials*. https://doi.org/10.3390/ma14206094 (2021).
4. Onat, N. & Kucukvar, M. Carbon footprint of construction industry: A global review and supply chain analysis. *Renew. Sustain. Energy Rev*. https://doi.org/10.1016/j.rser.2020.109783 (2020).
5. Osorio-Gomez, C., Alzate-Buitrago, A., Amariles-López, C., Aristizábal-Torres, D. & Mancilla-Rico, E. Interaction of life cycle assessment (LCA) and BIM in a construction project to reduce the environmental footprint. *Civil Eng. J.* https://doi.org/10.28991/cej-2025-011-01-08 (2025).
6. Labaran, Y., Mathur, V., Muhammad, S. & Musa, A. Carbon footprint management: A review of construction industry. *Clean. Eng. Technol.* https://doi.org/10.1016/j.clet.2022.100531 (2022).
7. Dolmatov, S., Kolesnikov, P. & Smertin, N. Methods for reducing the carbon footprint of industrial and construction facilities. *IOP Conf. Series: Earth Environ. Sci.* https://doi.org/10.1088/1755-1315/981/4/042005 (2022).
8. Yardimci, Y. & Kuruçay, E. LCA-TOPSIS integration for minimizing material waste in the construction sector: A BIM-Based Decision-Making. *Buildings* https://doi.org/10.3390/buildings14123919 (2024).
9. Akan, M., Dhavale, D. & Sarkis, J. Greenhouse gas emissions in the construction industry: an analysis and evaluation of a concrete supply chain. *J. Clean. Prod.*. https://doi.org/10.1016/J.JCLEPRO.2017.07.225 (2017).
10. Labaran, Y., Musa, A., Mathur, V. & Saini, G. Exploring the carbon footprint of nigeria's construction sector: a quantitative insight. *Environ. Dev. Sustain.* https://doi.org/10.1007/s10668-024-05111-5 (2024).
11. Yang, Z., Zhang, B., Yang, Y., Qin, B. & Wang, Z. Interprovincial inequality between economic benefit and carbon footprint: perspective from china's construction industry. *Environ. Impact Assess. Rev.* https://doi.org/10.1016/j.eiar.2023.107293 (2024).
12. Chaudhury, S., Sharma, R., Thapliyal, U., Singh, L. & P., & Low-CO2 emission strategies to achieve net zero target in cement sector. *J. Clean. Prod.* https://doi.org/10.1016/j.jclepro.2023.137466 (2023).
13. Ahmad, M., Fernández-Jiménez, A., Chen, B., Leng, Z. & Dai, J. Low-carbon cementitious materials: Scale-up potential, environmental impact and barriers. *Constr. Build. Mater.* https://doi.org/10.1016/j.conbuildmat.2024.139087 (2024).
14. Dunant, C., Joseph, S., Prajapati, R. & Allwood, J. Electric recycling of Portland cement at scale. *Nature*. https://doi.org/10.1038/s41586-024-07338-8 (2024).
15. Wang, W., Ye, M., Shi, Y. & Xiao, D. Plant-level intensity of energy and CO2 emissions for Portland cement in Guizhou of Southwest China 2019–2022. *Sci. Data*. https://doi.org/10.1038/s41597-024-03621-5 (2024).
16. Meng, D., Unluer, C., Yang, E. & Qian, S. Recent advances in magnesium-based materials: CO2 sequestration and utilization, mechanical properties and environmental impact. *Cem. Concr. Compos.* https://doi.org/10.1016/j.cemconcomp.2023.104983 (2023).
17. Ige,O., Olanrewaju, O., Duffy, K. & Collins, O. Environmental impact analysis of Portland cement (CEM1) using the midpoint method. *Energies* **15**, 2708 (2022). https://doi.org/10.3390/en15072708
18. Sánchez, A., Ramos, V., Polo, M., Ramón, M. & Utrilla, J. Life cycle assessment of cement production with marble waste sludges. *Int. J. Environ. Res. Public Health*. https://doi.org/10.3390/ijerph182010968 (2021).
19. Tarpani, R. et al. Environmental assessment of cement production with added graphene. *Clean. Environ. Syst.* https://doi.org/10.1016/j.cesys.2024.100206 (2024).
20. Sousa, V., Bogas, J., Real, S. & Meireles, I. Industrial production of recycled cement: energy consumption and carbon dioxide emission Estimation. *Environ. Sci. Pollut. Res.*. https://doi.org/10.1007/s11356-022-20887-7 (2022).
21. Neupane, K. Evaluation of environmental sustainability of One-part geopolymer binder concrete. *Clean. Mater.* https://doi.org/10.1016/j.clema.2022.100138 (2022).
22. Singh, N. & Middendorf, B. Geopolymers as an alternative to Portland cement: An overview. *Constr. Build. Mater.*. https://doi.org/10.1016/j.conbuildmat.2019.117455 (2020).
23. Jalal, P., Srivastava, V. & Tiwari, A. Geopolymer concrete: an alternative to conventional concrete for sustainable construction. *J. Environ. Nanatechnol.* https://doi.org/10.13074/jent.2024.12.2441122 (2024).
24. Farooq, F. et al. GPCas sustainable material: A state of the Art review. *Constr. Build. Mater.* https://doi.org/10.1016/j.conbuildmat.2021.124762 (2021).
25. Oyebisi, S. et al. Sustainability assessment of gpcsynthesized by slag and corncob Ash. *Case Stud. Constr. Mater.* https://doi.org/10.1016/j.cscm.2022.e01665 (2022).
26. Amran, Y., Alyousef, R., Alabduljabbar, H. & MohamedEl Clean production and properties of geopolymer concrete; A review. *J. Clean. Prod.*. https://doi.org/10.1016/j.jclepro.2019.119679 (2020).
27. Ikotun, J., Aderinto, G., Madirisha, M. & Katte, V. Geopolymer cement in pavement applications: bridging sustainability and performance. *Sustainability* https://doi.org/10.3390/su16135417 (2024).
28. Nodehi, M. & Taghvaee, V. Alkali-Activated materials and geopolymer: a review of common precursors and activators addressing circular economy. *Circular Econ. Sustain.*. https://doi.org/10.1007/s43615-021-00029-w (2021).
29. Ahmed, H. et al. GPCas a cleaner construction material: an overview on materials and structural performances. *Clean. Mater.* https://doi.org/10.1016/j.clema.2022.100111 (2022).
30. Verma, M. et al. Geopolymer concrete: A material for sustainable development in Indian construction industries. *Crystals* https://doi.org/10.3390/cryst12040514 (2022).
31. Meskhi, B. et al. *Anal. Rev. Geopolymer Concrete: Retrospective Curr. Issues Mater.*. https://doi.org/10.3390/ma16103792 (2023).
32. Amin,M., Elsakhawy, Y., El-hassan, K. & Abdelsalam, B. Behavior evaluation of sustainable high strength GPCbased on fly ash, metakaolin, and slag. *Case Stud. Constr. Mater.* **16**, e00976 (2022). https://doi.org/10.1016/j.cscm.2022.e00976
33. Wasim, M., Ngo, T. & Law, D. A state-of-the-art review on the durability of GPCfor sustainable structures and infrastructure. *Constr. Build. Mater.* https://doi.org/10.1016/J.CONBUILDMAT.2021.123381 (2021).
34. Chen, K., Wu, D., Xia, L., Cai, Q. & Zhang, Z. GPCdurability subjected to aggressive environments – A review of influence factors and comparison with ordinary Portland cement. *Constr. Build. Mater.*. https://doi.org/10.1016/J.CONBUILDMAT.2021.122496 (2021).

35. Almutairi, A., Tayeh, B., Adesina, A., Isleem, H. & Zeyad, A. Potential applications of GPCin construction: A review. *Case Stud. Constr. Mater.* https://doi.org/10.1016/j.cscm.2021.e00733 (2021).
36. Delgado-Plana,P., Bueno-Rodríguez, S., Pérez-Villarejo, L. & Eliche-Quesada, D. Effect of Portland Cement Addition in Ferrosilicon Slag Alkali Activated Materials. *Mater. Proc.* **8**, 122 (2022). https://doi.org/10.3390/materproc2022008122
37. Khoroshev, A., Makarevich, A., Chernyshev, S., Lesyuk, V. & Shishlov, A. Use of ferrosilicon slag in steel production. *Metallurgist.* https://doi.org/10.1007/s11015-022-01356-5 (2022).
38. Hou, Y., Zhang, G. & Chou, K. Reaction behavior of SiC with CaO–SiO2–Al2O3 slag. *ISIJ Int.* https://doi.org/10.2355/ISIJINTERNATIONAL.ISIJINT-2020-605 (2021).
39. Kim, H. & Ann, K. Applicability of ferrosilicon slag for a cementitious binder in concrete mix. *Constr. Build. Mater.*. https://doi.org/10.1016/j.conbuildmat.2020.121873 (2021).
40. Ahmed, M. et al. Fabrication of thermal insulation geopolymer bricks using ferrosilicon slag and alumina waste. *Case Stud. Constr. Mater.* https://doi.org/10.1016/j.cscm.2021.e00737 (2021).
41. Amin, M., Zeyad, A., Tayeh, B. & Agwa, I. Effect of ferrosilicon and silica fume on mechanical, durability, and microstructure characteristics of ultra high-performance concrete. *Constr. Build. Mater.* https://doi.org/10.1016/j.conbuildmat.2021.126233 (2022).
42. Tayeh, B., Hakamy, A., Amin, M., Zeyad, A. & Agwa, I. Effect of air agent on mechanical properties and microstructure of lightweight gpcunder high temperature. *Case Stud. Constr. Mater.* https://doi.org/10.1016/j.cscm.2022.e00951 (2022).
43. Chen, Z. H., Ba, Y., Shao, N. & M., & Properties of alkali activated materials prepared with secondary aluminum Ash sintered powder. *Constr. Build. Mater.* https://doi.org/10.1016/j.conbuildmat.2024.139516 (2025).
44. Zhang, S., Wang, K., Li, H., Zhang, X. & Jiang, Y. Novel SCMs produced by the calcination of secondary aluminium Dross with dolomite and their potential usage in cemented paste backfill. *Constr. Build. Mater.* https://doi.org/10.1016/j.conbuildmat.2022.130119 (2023).
45. Singh, G. & Scrivener, K. Performance of limestone calcined clay cement (LC3)-Based lightweight blocks. RILEM Bookseries. (2020). https://doi.org/10.1007/978-981-15-2806-4_94
46. Hameed, S. et al. Effect of aluminium waste powder on the strength properties of cement mortar. *Neutron* **23**, 1 (2023).
47. Gharieb, M. & Khater, H. Valorization study of mixing aluminum slag with binary geopolymer blends to produce lightweight geopolymer concrete. *Constr. Build. Mater.* https://doi.org/10.1016/j.conbuildmat.2025.140288 (2025).
48. Abdellatief, M. et al. Physico-mechanical, thermal insulation properties, and microstructure of geopolymer foam concrete containing sawdust Ash and egg shell. *J. Building Eng.* https://doi.org/10.1016/j.jobe.2024.109374 (2024).
49. Sanjayan, J., Nazari, A., Chen, L. & Nguyen, G. Physical and mechanical properties of lightweight aerated geopolymer. *Constr. Build. Mater.* https://doi.org/10.1016/J.CONBUILDMAT.2015.01.043 (2015).
50. Font, A., Borrachero, M., Soriano, L., Monzó, J. & Payá, J. Geopolymer eco-cellular concrete (GECC) based on fluid catalytic cracking catalyst residue (FCC) with addition of recycled aluminium foil powder. *J. Clean. Prod.* https://doi.org/10.1016/J.JCLEPRO.2017.09.110 (2017).
51. Keawpapasson, P. et al. Metakaolin-Based porous geopolymer with aluminium powder. *Key Eng. Mater.* https://doi.org/10.4028/www.scientific.net/KEM.608.132 (2014).
52. Hajimohammadi, A., Ngo, T. & Mendis, P. How does aluminium foaming agent impact the geopolymer formation mechanism. *Cement Concr. Compos.*. https://doi.org/10.1016/J.CEMCONCOMP.2017.03.022 (2017).
53. Durak, U. The improvement of strength and microstructural properties of fly ash-based geopolymer by adding elemental aluminum powder. *J. Mater. Cycles Waste Manage.*. https://doi.org/10.1007/s10163-022-01520-8 (2022).
54. Hajimohammadi, A., Ngo, T. & Mendis, P. The effect of aluminium reaction on formation mechanism and structural properties of geopolymers. (2016).
55. Matei, E. et al. Ferrous industrial Wastes—Valuable resources for water and wastewater decontamination. *Int. J. Environ. Res. Public Health*. https://doi.org/10.3390/ijerph192113951 (2022).
56. Jiménez, A. et al. Synthesis of pollucite and analcime zeolites by recovering aluminum from a saline slag. *J. Clean. Prod.*. https://doi.org/10.1016/J.JCLEPRO.2021.126667 (2021).
57. Veliyev, E. & Aliyev, A. Design of a lightweight cementing material on basis of geopolymer and gas-forming agent. SOCAR Proceedings. (2023). https://doi.org/10.5510/ogp20230100813
58. Kanagaraj, B., Anand, N., Andrushia, A. D. & Lubloy, E. Investigation on engineering properties and micro-structure characteristics of low strength and high strength geopolymer composites subjected to standard temperature exposure. *Case Stud. Constr. Mater.* https://doi.org/10.1016/j.cscm.2022.e01608 (2022).
59. Mostafa, S., Agwa, I., Elboshy, B., Zeyad, A. & Hassan, A. The effect of lightweight GPC containing air agent on Building envelope performance and internal thermal comfort. *Case Stud. Constr. Mater.* https://doi.org/10.1016/j.cscm.2024.e03365 (2024).
60. Kioupis, D., Skaropoulou, A., Tsivilis, S. & Kakali, G. Development of lightweight geopolymer composites by combining various CDW streams. *Ceramics* https://doi.org/10.3390/ceramics6020048 (2023).
61. Lima, J. et al. Use of rice husk Ash to produce alternative sodium silicate for geopolymerization reactions. *Cerâmica* https://doi.org/10.1590/0366-69132021673812891 (2021).
62. Hou, D. et al. Molecular insights into the reaction process of Alkali-Activated Metakaolin by sodium hydroxide. *Langmuir: ACS J. Surf. Colloids*. https://doi.org/10.1021/acs.langmuir.2c01631 (2022).
63. Tong, K., Vinai, R. & Soutsos, M. Use of Vietnamese rice husk Ash for the production of sodium silicate as the activator for alkali-activated binders. *J. Clean. Prod.* https://doi.org/10.1016/J.JCLEPRO.2018.08.025 (2018).
64. Karaaslan, C. & Yener, E. The effect of alkaline activator components on the properties of fly Ash added pumice based geopolymer. *J. Inst. Sci. Technol.* https://doi.org/10.21597/JIST.840872 (2021).
65. Li, H., Li, J. & Lu, Z. Effect of Na/Al on formation, structures and properties of Metakaolin based Na-geopolymer. *Constr. Build. Mater.* https://doi.org/10.1016/J.CONBUILDMAT.2019.07.171 (2019).
66. Rihan, M., Alahmari, T., Onchiri, R., Gathimba, N. & Sabuni, B. Impact of alkaline concentration on the mechanical properties of GPCMade up of fly Ash and sugarcane Bagasse Ash. *Sustainability* https://doi.org/10.3390/su16072841 (2024).
67. Venkatesan, G., Alengaram, U., Ibrahim, S. & Ibrahim, M. Effect of fly Ash characteristics, sodium-based alkaline activators, and process variables on the compressive strength of siliceous fly Ash geopolymers with microstructural properties: A comprehensive review. *Constr. Build. Mater.* https://doi.org/10.1016/j.conbuildmat.2024.136808 (2024).
68. Shilar,F., Ganachari, S., Patil, V., Khan, T. & Dawood, S. Molarity activity effect on mechanical and microstructure properties of geopolymer concrete: A review. *Case Stud. Constr. Mater.* **16**, e01014 (2022). https://doi.org/10.1016/j.cscm.2022.e01014
69. Bidwe,S. S. & Hamane, A. A. Effect of different molarities of sodium hydroxide solution on the strength of geopolymer concrete. *Am. J. Eng. Res.* **4**, 139 (2015). https://doi.org/10.6084/M9.FIGSHARE.1390492.V1
70. Pane,I., Imran, I. & Budiono, B. Compressive strength of fly ash-based GPCwith a variable of sodium hydroxide (NaOH) solution molarity. *MATEC Web Conf.* **147**, 01004 (2018). https://doi.org/10.1051/MATECCONF/201814701004
71. Mortar,N., Kamarudin, H., Rafiza, R., Meor, T. & Rosnita, M. Compressive strength of fly ash GPCby varying sodium hydroxide molarity and aggregate to binder ratio. io*P Conf. Series: Mater. Sci. Eng.* **864**, 012037 (2020). https://doi.org/10.1088/1757-899X/864/1/012037
72. Memon, F. et al. Effect of sodium hydroxide concentration on fresh properties and compressive strength of self-compacting geopolymer concrete. *J. Eng. Sci. Technol.* **8**, 44 (2013).

73. Reddy, S., Krishna, V., Rao, S. & Shrihari, S. Effect of molarity of sodium hydroxide and molar ratio of alkaline activator solution on the strength development of geopolymer concrete. *E3S Web Conferences*. https://doi.org/10.1051/e3sconf/202130901058 (2021).
74. Amarender, R. & Rayana, H. Study on the molarity effect of sodium hydroxide on gpcincorporating Nanosilica. *J. Phys: Conf. Ser.* https://doi.org/10.1088/1742-6596/2779/1/012040 (2024).
75. Ganesh, A. et al. Effect of molarity of sodium hydroxide solution over GGBS-based self compacting geopolymer concrete. *E3S Web Conferences*. https://doi.org/10.1051/e3sconf/202452901004 (2024).
76. Lavanya, G. & Jegan, J. Durability study on high calcium fly Ash based geopolymer concrete. *Adv. Mater. Sci. Eng.* https://doi.org/10.1155/2015/731056 (2015).
77. Nikolov, A. Alkali-activated geopolymers based on iron-rich slag from copper industry. *IOP Conf. Series: Mater. Sci. Eng.* https://doi.org/10.1088/1757-899X/951/1/012006 (2020).
78. Simon, S. et al. The fate of iron during the alkali-activation of synthetic (CaO-)FeOx-SiO2 slags: an Fe K-edge XANES study. *J. Am. Ceram. Soc.*. https://doi.org/10.1111/JACE.15354 (2018).
79. Nikolov, A. Alkali and acid activated geopolymers based on iron-silicate fines - by-product from copper industry. *Int. Sci. J. Mach. Technol. Mater.* **14**, 37 (2020).
80. Kanagaraj, B., Lubloy, E., Anand, N., Hlavicka, V. & Kiran, T. Investigation of physical, chemical, mechanical, and microstructural properties of cement-less concrete–state-of-the-art review. *Constr. Build. Mater.* https://doi.org/10.1016/j.conbuildmat.2022.130020 (2023).
81. Wu, J. Study on the effect of different air-entraining agents on the properties of concrete. *E3S Web Conferences*. https://doi.org/10.1051/e3sconf/202561802001 (2025).
82. Song, X., Ng, S., Ni, T., Wang, Y. & Ke, F. Effect of air entraining agents on the air void structure of concrete. *J. Phys: Conf. Ser.*. https://doi.org/10.1088/1742-6596/2011/1/012051 (2021).
83. Yang, Y. Study on the influence of Air-Entraining agent on concrete pore structure based on nuclear magnetic resonance technology. *Acad. J. Sci. Technol.* https://doi.org/10.54097/evveb837 (2025).
84. Paruthi, S., Rahman, I., Husain, A., Hasan, M. A. & Khan, A. H. Effects of chemicals exposure on the durability of geopolymer concrete incorporated with silica fumes and nano-sized silica at varying curing temperatures. *Materials* https://doi.org/10.3390/ma16186332 (2023).
85. Lee, Y. H. et al. Thermal performance of structural lightweight concrete composites for potential energy saving. *Crystals* https://doi.org/10.3390/cryst11050461 (2021).
86. Chaabene, W., Flah, M. & Nehdi, M. Machine learning prediction of mechanical properties of concrete: critical review. *Constr. Build. Mater.* https://doi.org/10.1016/j.conbuildmat.2020.119889 (2020).
87. Vatin, N., Hematibahar, M. & Gebre, T. Chopped and minibars reinforced high-performance concrete: machine learning prediction of mechanical properties. *Front. Built Environ.* https://doi.org/10.3389/fbuil.2025.1558394 (2025).
88. Asteris, P., Skentou, A., Bardhan, A., Samui, P. & Pilakoutas, K. Predicting concrete compressive strength using hybrid ensembling of surrogate machine learning models. *Cem. Concr. Res.* https://doi.org/10.1016/J.CEMCONRES.2021.106449 (2021).
89. Imran, M., Amjad, H., Khan, S. & Ali, S. Machine learning assisted prediction of the mechanical properties of carbon nanotube-incorporated concrete. *Struct. Concrete*. https://doi.org/10.1002/suco.202400727 (2024).
90. Liu, Y. High-Performance concrete strength prediction based on machine learning. *Comput. Intell. Neurosci.*. https://doi.org/10.1155/2022/5802217 (2022).
91. Kashem, A. et al. Hybrid data-driven approaches to predicting the compressive strength of ultra-high-performance concrete using SHAP and PDP analyses. *Case Stud. Constr. Mater.* https://doi.org/10.1016/j.cscm.2024.e02991 (2024).
92. Pal, A., Ahmed, K., Hossain, F. & Alam, M. Machine learning models for predicting compressive strength of fiber-reinforced concrete containing waste rubber and recycled aggregate. *J. Clean. Prod.* https://doi.org/10.1016/j.jclepro.2023.138673 (2023).
93. Hosseinzadeh, M., Dehestani, M. & Hosseinzadeh, A. Prediction of mechanical properties of recycled aggregate fly Ash concrete employing machine learning algorithms. *J. Building Eng.* https://doi.org/10.1016/j.jobe.2023.107006 (2023).
94. Çiftçioğlu, Ö., Kazemi, F. & Shafighfard, T. Grey Wolf optimizer integrated within boosting algorithm: application in mechanical properties prediction of ultra high-performance concrete including carbon nanotubes. *Appl. Mater. Today*. https://doi.org/10.1016/j.apmt.2025.102601 (2025).
95. Moein, M. et al. Predictive models for concrete properties using machine learning and deep learning approaches: A review. *J. Building Eng.* https://doi.org/10.1016/j.jobe.2022.105444 (2022).
96. Koya, B., Aneja, S., Gupta, R. & Valeo, C. Comparative analysis of different machine learning algorithms to predict mechanical properties of concrete. *Mech. Adv. Mater. Struct.*. https://doi.org/10.1080/15376494.2021.1917021 (2021).
97. Zhang, L. & Zhao, Y. Calculation of the mechanical properties of high-performance concrete employing hybrid and ensemble-hybrid techniques. *Struct. Concrete*. https://doi.org/10.1002/suco.202300418 (2024).
98. Kumar, R., Rai, B. & Samui, P. Prediction of mechanical properties of high-performance concrete and ultrahigh-performance concrete using soft computing techniques: A critical review. *Struct. Concrete*. https://doi.org/10.1002/suco.202400188 (2024).
99. Hematibahar, M. et al. Analysis of models to predict mechanical properties of High-Performance and Ultra-High-Performance concrete using machine learning. *J. Compos. Sci.* https://doi.org/10.3390/jcs8080287 (2024).
100. Hafez, H., Teirelbar, A., Kurda, R., Tošić, N. & De La Fuente, A. Pre-bcc: A novel integrated machine learning framework for predicting mechanical and durability properties of blended cement concrete. *Constr. Build. Mater.* https://doi.org/10.1016/j.conbuildmat.2022.129019 (2022).
101. Hosseinzadeh, M., Samadvand, H., Hosseinzadeh, A., Mousavi, S. & Dehestani, M. Concrete strength and durability prediction through deep learning and artificial neural networks. *Front. Struct. Civil Eng.* https://doi.org/10.1007/s11709-024-1124-9 (2024).
102. Zhang, M. & Kang, R. Machine learning methods for predicting the durability of concrete materials: A review. *Adv. Cem. Res.* https://doi.org/10.1680/jadcr.24.00133 (2025).
103. Gamil,Y. Machine learning in concrete technology: A review of current researches, trends, and applications. *Front. Built Environ.* **9**, 1145591 (2023). https://doi.org/10.3389/fbuil.2023.1145591
104. Arasteh-Khoshbin, O., Seyedpour, S., Mandl, L., Lambers, L. & Ricken, T. Comparing durability and compressive strength predictions of hyperoptimized random forests and artificial neural networks on a small dataset of concrete containing nano SiO2 and RHA. *Eur. J. Environ. Civil Eng.*. https://doi.org/10.1080/19648189.2024.2393881 (2024).
105. Upreti, K. et al. Prediction of mechanical strength by using an artificial neural network and random forest algorithm. *J. Nanomaterials*. https://doi.org/10.1155/2022/7791582 (2022).
106. Wang, L., Wu, X., Chen, H. & Zeng, T. Prediction of impermeability of the concrete structure based on random forest and support vector machine. *IOP Conf. Series: Earth Environ. Sci.*. https://doi.org/10.1088/1755-1315/552/1/012004 (2020).
107. Xu, Y. et al. Computation of High-Performance concrete compressive strength using standalone and ensembled machine learning techniques. *Materials*. https://doi.org/10.3390/ma14227034 (2021).
108. Kushal, B., Goud, K., Kumar, K. & Mohan, U. Performance prediction of Eco-Friendly concrete with artificial neural networks (ANNs). *E3S Web Conferences*. https://doi.org/10.1051/e3sconf/202459601021 (2024).
109. Farooq, F. et al. A comparative study of random forest and genetic engineering programming for the prediction of compressive strength of high strength concrete (HSC). *Appl. Sci.* https://doi.org/10.3390/app10207330 (2020).

110. Chen, P., Wang, H., Cao, S. & Lv, X. Prediction of mechanical behaviours of FRP-Confined circular concrete columns using artificial neural network and support vector regression: modelling and performance evaluation. *Materials*. https://doi.org/10.3390/ma15144971 (2022).
111. Lunardi, L., Cornélio, P., Prado, L., Nogueira, C. & Félix, E. Hybrid machine learning model for predicting the fatigue life of plain concrete under Cyclic compression. *Buildings* https://doi.org/10.3390/buildings15101618 (2025).
112. Pfeiffer, O. et al. Bayesian design of concrete with amortized Gaussian processes and multi-objective optimization. *Cem. Concr. Res.* https://doi.org/10.1016/j.cemconres.2023.107406 (2024).
113. Yuan, Z., Zheng, W. & Qiao, H. Machine learning based optimization for mix design of manufactured sand concrete. *Constr. Build. Mater.* https://doi.org/10.1016/j.conbuildmat.2025.140256 (2025).
114. Chen, B. et al. Optimization of high-performance concrete mix ratio design using machine learning. *Eng. Appl. Artif. Intell.*. https://doi.org/10.1016/j.engappai.2023.106047 (2023).
115. Wang, M. et al. Multi-objective optimization of ultra-high performance concrete based on life-cycle assessment and machine learning methods. *Front. Struct. Civil Eng.* https://doi.org/10.1007/s11709-025-1152-0 (2025).
116. Wakjira, T., Kutty, A. & Alam, M. A novel framework for developing environmentally sustainable and cost-effective ultra-high-performance concrete (UHPC) using advanced machine learning and multi-objective optimization techniques. *Constr. Build. Mater.* https://doi.org/10.1016/j.conbuildmat.2024.135114 (2024).
117. Liu, J., Liu, F. & Wang, L. Automated, economical, and environmentally-friendly asphalt mix design based on machine learning and multi-objective grey Wolf optimization. *J. Traffic Transp. Eng. (English Edition)*. https://doi.org/10.1016/j.jtte.2023.10.002 (2024).
118. Pham, T., Le-Hong, T. & Tran, X. Efficient Estimation and optimization of Building costs using machine learning. *Int. J. Constr. Manag.*. https://doi.org/10.1080/15623599.2021.1943630 (2021).
119. Arabani, M., Effati, M., Safari, M., Shalchian, M. M. & Hassanjani, M. H. The comprehensive review on the mechanisms and performance of different bio-extenders in the bitumen. *Int. J. Pavement Res. Technol.* https://doi.org/10.1007/s42947-024-00457-5 (2024).
120. Hassanjani, M. H., Arabani, M., Shalchian, M. M. & Amiri, A. Evaluation of different biomass conversion methods to bio-oil for partial replacement of petroleum bitumen: analysis of effects and implications. *Int. J. Pavement Eng.* https://doi.org/10.1080/10298436.2025.2472860 (2025).
121. Arabani, M., Hassanjani, M. H., Farkhondeh, J. & Taleghani, M. Y. Enhancing mechanical properties of hot mix asphalt with Olive kernel ash: A sustainable modifier. *Constr. Build. Mater.* https://doi.org/10.1016/j.conbuildmat.2024.138740 (2024).
122. Arabani, M., Sadeghnejad, M., Haghanipour, J. & Hassanjani, M. H. The influence of rice Bran oil and nano-calcium oxide into bitumen as sustainable modifiers, case stud. *Construct Mater.* https://doi.org/10.1016/j.cscm.2024.e03458 (2024).
123. McLellan, B. C., Williams, R. P., Lay, J., van Riessen, A. & Corder, G. D. Costs and carbon emissions for geopolymer pastes in comparison to ordinary Portland cement. *J. Clean. Prod.* https://doi.org/10.1016/j.jclepro.2011.02.010 (2011).
124. Norgate, T. E. & Rankin, W. J. The role of metals in sustainable development. In: Green Processing 2002. Carlton, Australia: AusIMM; (2002).
125. Turner, L. K. & Collins, F. G. Carbon dioxide equivalent (CO_2-e) emissions: A comparison between geopolymer and OPC cement concrete. *Constr. Build. Mater.* https://doi.org/10.1016/j.conbuildmat.2013.01.023 (2013).
126. Duxson, P., Provis, J. L., Lukey, G. C. & van Deventer, J. S. J. The role of inorganic polymer technology in the development of 'green concrete'. *Cem. Concr Res.* https://doi.org/10.1016/j.cemconres.2007.08.018 (2007).
127. Flower, D. J. M. & Sanjayan, J. G. Greenhouse gas emissions due to concrete manufacture. *Int. J. Life Cycle Assess.* https://doi.org/10.1065/lca2007.05.327 (2007).

Author contributions

K. Narshimha Raju : Investigation, methodology, visualization, writing—original draft.**G. K. Arunvivek** : conceptualization, methodology, validation, review and editing.

Funding

The authors declare that no funding/grants were received during this project and preparation of this manuscript.

Declarations

Competing interests

The authors declare no competing interests.

Additional information

Correspondence and requests for materials should be addressed to K.N.R.